APPLIED SCIENCES AND ENGINEERING

Autonomously designed free-form 2D DNA origami

Hyungmin Jun[1]*, Fei Zhang[2]*, Tyson Shepherd[1], Sakul Ratanalert[1,3], Xiaodong Qi[2], Hao Yan[2], Mark Bathe[1†]

Scaffolded DNA origami offers the unique ability to organize molecules in nearly arbitrary spatial patterns at the nanometer scale, with wireframe designs further enabling complex 2D and 3D geometries with irregular boundaries and internal structures. The sequence design of the DNA staple strands needed to fold the long scaffold strand to the target geometry is typically performed manually, limiting the broad application of this materials design paradigm. Here, we present a fully autonomous procedure to design all DNA staple sequences needed to fold any free-form 2D scaffolded DNA origami wireframe object. Our algorithm uses wireframe edges consisting of two parallel DNA duplexes and enables the full autonomy of scaffold routing and staple sequence design with arbitrary network edge lengths and vertex angles. The application of our procedure to geometries with both regular and irregular external boundaries and variable internal structures demonstrates its broad utility for nanoscale materials science and nanotechnology.

INTRODUCTION

Classically known for its role as the core storage element of genetic information, reliable Watson-Crick base pairing and synthetic sequence control also render DNA a versatile material for structured nanoscale materials engineering. Following the conception of the immobile four-way junction (*1*), structural DNA nanotechnology has blossomed to include myriad design approaches to synthesize complex two-dimensional (2D) and 3D static and dynamic nanoscale objects (*2*–*15*). In particular, scaffolded DNA origami (*3*) was a discrete technological advance that enabled the ability to produce monodisperse DNA products on the megadalton scale with high folding efficiency by leveraging the use of a long single-stranded DNA (ssDNA) scaffold that is annealed with short complementary oligonucleotide staple strands to yield a target shape. While the scaffold length technically limits the size of a single origami object, supra-origami assemblies may also be formed from constituent subunits (*14*). Nondiscrete structural assemblies may also be formed using single-stranded tiles (*16*, *17*), which have been applied to generate micrometer-scale DNA origami arrays to render complex images via fractal assembly (*18*). Precise control over nanoscale structure has afforded the broad application of scaffolded and nonscaffolded DNA origami to template carbon nanotubes (*19*) and metallic nanoparticles (*20*); fabricate metallic nanowires and nanoparticles (*21*–*24*); coordinate biomolecules (*22*), graphene sheets (*25*), and cell ligand patterns (*26*); form single-molecule chemical reactors (*27*); and control nanoscale energy transport (*28*); as well as program smart vehicles for drug delivery (*29*, *30*) and perform complex lithography (*31*, *32*). These applications rely on the combined structural stiffness and stability of DNA origami particles and the ability to perform nearly arbitrary chemical functionalization at predefined staple locations. With recent advances in enzymatic (*11*, *33*) and bacterial scaffold (*34*) synthesis that now enable large-scale, low-cost origami production with sequence control, a major remaining bottleneck for the field is the democratization of scaffolded DNA origami design via autonomous sequence design algorithms.

Conventionally, ssDNA scaffold routing and staple sequence design needed for scaffolded DNA origami synthesis are performed manually for each target object of interest in a laborious process that is facilitated by visualization software such as caDNAno (*4*, *35*) or Tiamat (*36*). However, the lack of systematic design rules for staple sequence design and the ad hoc manual scaffold routing through each base pair in a target object limits the use of scaffolded DNA origami to experts in the field. While 3D polygonal objects have been rendered semiautomatically (*10*) and automatically (*11*) from the top-down based on target surface geometries, equivalent solutions for 2D free-form geometries are lacking, with the exception of one semiautomated approach (*37*). However, this approach relies on more flexible, single duplex DNA edges and semisupervised, iterative sequence and edge length design to render approximately target wireframe geometries, and while the 3D algorithm DAEDALUS (*11*) can be used to render arbitrary target 3D objects, it is incapable of rendering 2D planar geometries or programming arbitrary edge lengths and vertex angles. Therefore, no general solution exists for the fully autonomous sequence design of free-form 2D scaffolded DNA origami for wireframe assemblies.

To enable any materials scientist or engineer to generate wireframe 2D origami objects of fully customized shape, here we introduce a fully automatic inverse design procedure that programs arbitrary 2D DNA assemblies by using dual DNA duplex edges of arbitrary length based on antiparallel double (DX) crossovers with multiarm junctions at vertices. Unlike a previous top-down approach (*11*) that used discrete edge lengths, our procedure enables entirely free-form design, allowing users to provide input with freehand drawing of only the border shape of the target object, with the internal structure determined automatically. Alternatively, internal geometry may also be specified for automatic rendering as DX-based edges in the final origami object (movies S1 to S3). We demonstrate our autonomous sequence design procedure with a variety of irregular and asymmetric objects including a range of different internal mesh patterns, edge lengths, and vertex types, which are validated using high-resolution atomic force microscopy (AFM) imaging. Our algorithmic approach, called PERDIX (Programmed Eulerian Routing for DNA Design using X-overs), is available for use online at http://perdix-dna-origami.org or as a stand-alone, open-source software.

[1]Department of Biological Engineering, Massachusetts Institute of Technology, 77 Massachusetts Avenue, Cambridge, MA 02139, USA. [2]The Biodesign Institute and School of Molecular Sciences, Arizona State University, Tempe, AZ 85287, USA. [3]Department of Chemical Engineering, Massachusetts Institute of Technology, 77 Massachusetts Avenue, Cambridge, MA 02139, USA.
*These authors contributed equally to this work.
†Corresponding author. Email: mark.bathe@mit.edu

RESULTS

Arbitrary 2D geometries are provided as input by drawing either only the border of the target object, whose interior is then rendered automatically by the algorithm, or the exact geometric lines that are then converted into DX edges in the final origami object (Fig. 1A and fig. S1).

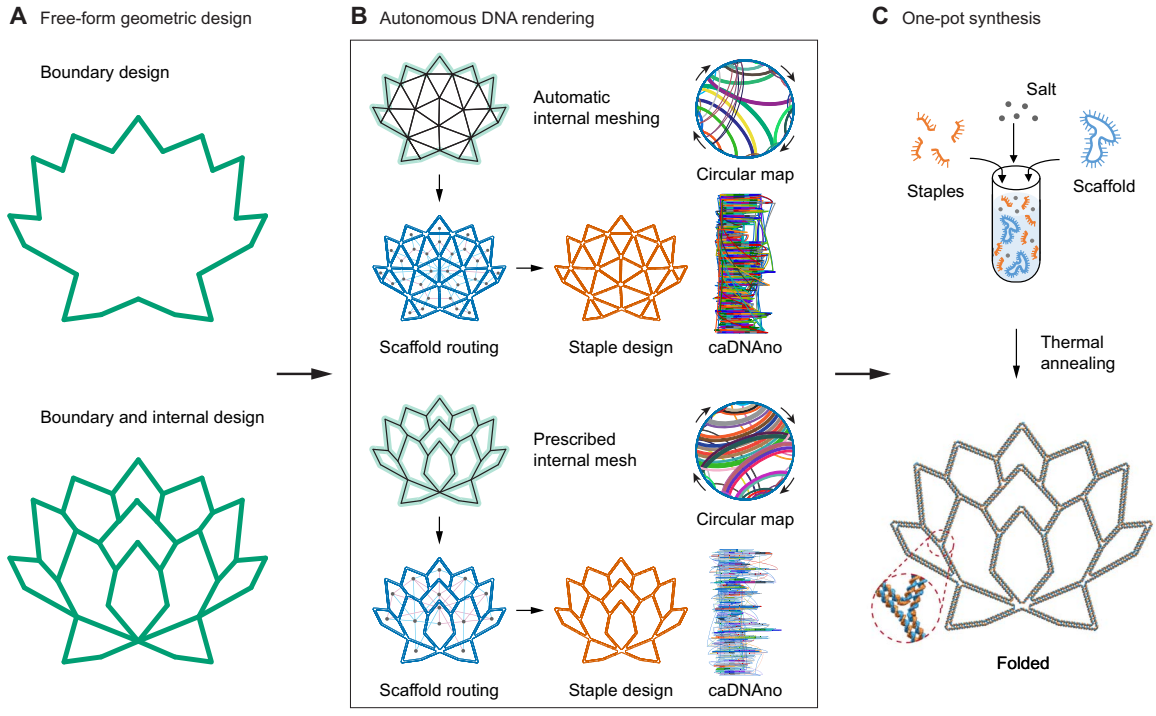

Fig. 1. Automated design of 2D wireframe scaffolded DNA origami objects. (**A**) Arbitrary target geometries can be specified in two ways: free-form boundary design (top), defining only the border of the target object, with the internal mesh geometry designed automatically, or free-form boundary and internal design (bottom), specifying the complete internal and external boundary geometry using piecewise continuous lines. (**B**) 2D line-based geometric representations are used as input to the algorithm that performs automatic scaffold and staple routings, converting each edge into two parallel duplexes joined by antiparallel crossovers. The single-stranded scaffold is routed throughout the entire origami object, with staple strands ranging in length from 20 to 60 nucleotides (nt; mean length, 40 nt). The circular maps illustrate the connectivities of staples hybridized to the circular scaffold in the final, self-assembled object, where each terminal point of the connecting staple line is located at the middle of its corresponding double-stranded DNA (dsDNA) domain in the folded line. caDNAno input files are also generated by the algorithm for manual editing of staple sequences or the scaffold routing path. (**C**) Staple sequences generated by the algorithm are used with the input scaffold to synthesize the programmed 2D wireframe object using standard one-pot thermal annealing.

In the former case [Fig. 1A (top) and fig. S1A], the interior geometry is meshed using triangles by DistMesh, an open-source meshing software that requires only a prespecified mesh density. For the latter case [Fig. 1A (bottom) and fig. S1], Shapely, a Python package for the manipulation and analysis of planar geometric objects, is used to generate the polygonal mesh in which the set of lines and their intersecting points form the target wireframe geometry. Offering these two distinct input free-form geometric specifications enables highly complex structures to be synthesized by nonexperts.

Having defined the target structure, a minimum edge length greater than or equal to 38 base pairs (bp) (12.58 nm) must be prescribed to ensure a target geometry with at least two double crossovers per edge, with the entire structure scaled accordingly. All target object lines are then converted automatically into DX edges with all vertices represented as multiarm junctions (Fig. 1B). The optimized scaffold routing based on graph theory is then generated automatically, and the sequence assignment of complementary staples is completed. A caDNAno (*35*) file is also generated as output to facilitate manual editing of topology and sequence. These output sequences can then be synthesized, mixed, and annealed to generate the designed object on the nanoscale with high geometric fidelity (Fig. 1C). Designed edges do not need to be an integral number of double helical turns of B-form DNA (10.5 bp), allowing for a broad design space compared with other approaches that requires discrete edge lengths based on the helicity of B-form DNA (*11*). This design flexibility is accomplished by introducing unpaired scaffold nucleotides to span the distance between the 3′ and 5′ ends between any incoming and outgoing edges, respectively, on a vertex-by-vertex basis, which would otherwise be misaligned due to the native twist of B-form DNA. The number of unpaired nucleotides present in each scaffold loop is chosen to be 0.42 nm per unpaired nucleotide based on previous work (*9*), where the number of unpaired nucleotides is computed from the Euclidean distance between the centroids of the two nucleotides spanning the vertex gap (see the Supplementary Materials).

To perform rapid and robust automatic sequence design in which the single-stranded circular DNA scaffold is routed through the entire origami object, we first translate all edges into DX motifs by rendering each edge of the target geometry using two antiparallel scaffold lines [Fig. 2A (step 1) and fig. S2, A to D]. These endpoints are then joined around one vertex so that every edge becomes part of a loop, resulting in one large outer loop containing numerous smaller loops for any target structure. Next, all possible positions for scaffold crossovers (fig. S3) are found between each neighboring loop pair to form the loop-crossover structure [Fig. 2A (step 2) and fig. S2E]. A Eulerian circuit through the entire structure is then realized by choosing a particular subset of double crossovers that ensures that every vertex contains an even number of duplexes and that the structure does not contain any internal closed scaffold loops.

To identify the subset of double crossovers that are used in the final structure, the dual graph of the loop-crossover structure is introduced

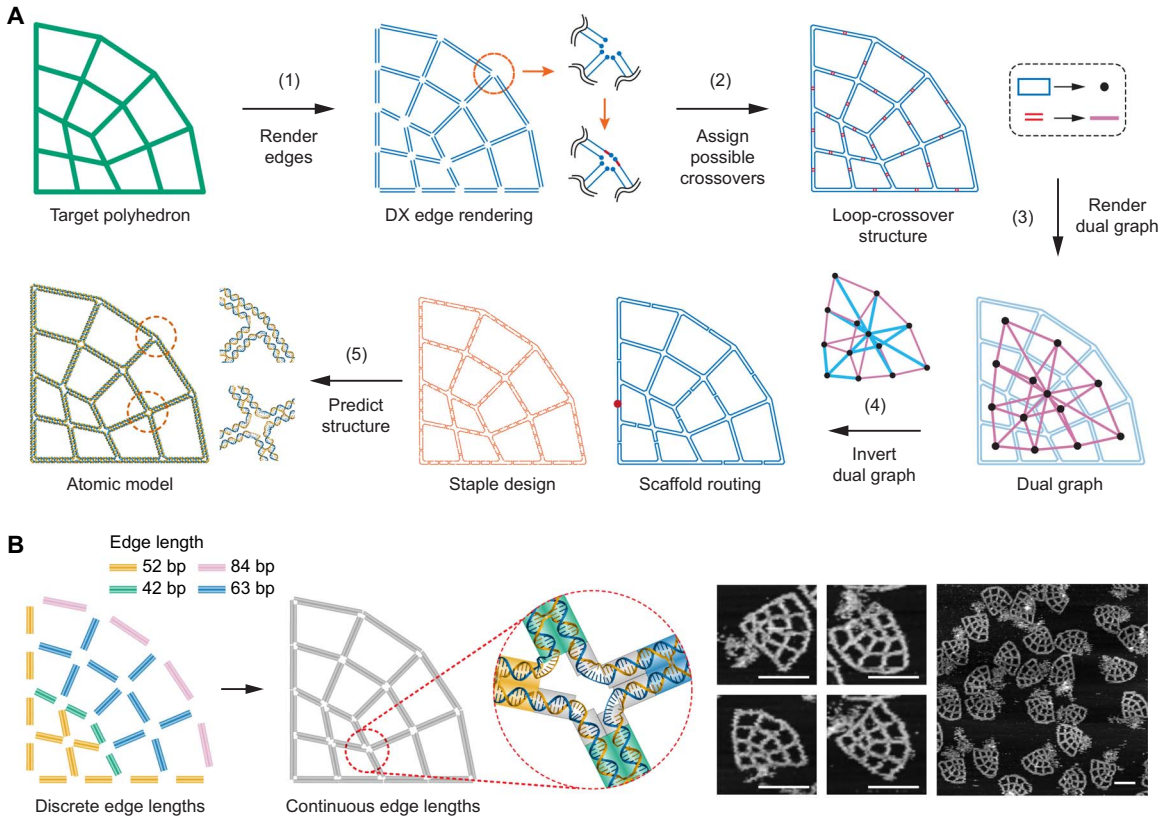

Fig. 2. Automatic scaffold routing and staple sequence design. (**A**) Step 1: Double-line segments representing two parallel B-form DNA duplexes are generated along the edges of the target wireframe geometry. Step 2: Endpoints are joined such that each duplex becomes part of a loop (blue) containing all possible scaffold double crossovers (red) between closed loops. Step 3: The dual graph of the loop-crossover structure is introduced by converting each loop into a node and each double crossover into an edge. Step 4: The spanning tree of the dual graph is computed and inverted to route the ssDNA scaffold throughout the entire origami object automatically (position of the scaffold nick is indicated by a solid red circle), which enables the assignment of complementary staple strands. Step 5: Last, a 3D atomic-level structural model is generated, assuming canonical B-form DNA duplexes. (**B**) Design using continuous edge length for asymmetric and irregular shapes. The target geometry can be modeled in two ways: Using a discrete edge length consisting of multiples of 10.5 bp rounded to the nearest nucleotide or a continuous edge length with no constraint on length. Continuous edge lengths enable the design of objects with arbitrary edge lengths, which require duplex extensions to fill gaps in vertices. Both edge types were experimentally tested by folding and visualizing with AFM (figs. S6 to S8). The highest folding yields occurred with continuous edge length particles with unpaired nucleotides at the vertices. Excess scaffold is apparent in the AFM images at the position of the scaffold nick indicated in the scaffold routing diagram in (A). Scale bars, 150 nm.

[Fig. 2A (step 3) and fig. S2F], in which each loop is represented by a node and each double crossover is referred to as an edge joining associated nodes. The spanning tree of this dual graph is then computed (fig. S2G) using Prim's algorithm, and the edges that are members of the spanning tree (labeled blue in the left panel) correspond to the subset of crossovers that are required to complete the Eulerian circuit. To complete the scaffold routing, the dual graph is inverted [Fig. 2A (step 4) and fig. S2H] back to the loop-crossover structure without the double crossovers corresponding to the nonmember's spanning tree. From the calculation of its spanning tree in the dual graph of the loop-crossover structure, the $N - 1$ double crossovers are determined, where N is the number of loops and each scaffold loop is connected to the neighboring loop through the selected double crossover, which results in the final scaffold loop specifying the entire target object. This dual graph approach contrasts with previous approaches in which the graph based on the edge-connectivity of the target polyhedron was used directly to compute the scaffold routing (*10*, *11*, *37*), ensuring that routing is fully automated using rules established previously yet implemented manually (*9*). Our spanning tree approach thereby offers fully automatic conversion of the input geometry to the full scaffold routing based on the single circuit that traverses each duplex only once. A linear scaffold nick position is assigned to ensure that it is noncoincident with crossovers and other nicks.

With the scaffold routing determined, complementary staple paths are introduced by assigning all permitted staple crossovers (fig. S3) on edges and connecting staples in vertices with unpaired poly(T) loops. The specific length of each poly(T) loop is determined on the basis of empirical values found to be optimal for the number of unpaired staple nucleotides in previous work (*9*). When the generated staple is circular, a nick is placed on the staple strand at the center of the longest dsDNA domain formed with the scaffold. Each noncircular staple is algorithmically subdivided to have a length ranging from 20 to 60 bases in the final rendering process (see the Supplementary Materials for design details). Having determined the regions of complementary staple and scaffold strands, staple sequences are computed using the Watson-Crick base pairing to the target scaffold sequence. The final structure is then converted into an atomic model for visualization and further analysis [Fig. 2A (step 5), fig. S2I, and movies S4 to S7].

In addition to solving the generalized scaffold routing problem in 2D, our approach offers the capability to design the lattice in such a

way as to extend one or both helices at each edge crossing to allow for a reduced gap at every vertex. This is accomplished by extending each helix to the intersection of its neighboring extended helix and spanning the remaining spatial gap between the two helices by the number of unpaired scaffold nucleotides necessary to maintain the vertex geometry (figs. S4 and S5). This extension of helices to join at vertices allows for completely arbitrary edge lengths that are not constrained to the 10.5-bp rule that has typically been used in DNA origami design (*3*, *11*). Further, this extension allows for arbitrary vertex angles to be formed between edges, which has not been algorithmically implemented prior to this work and has only been implemented manually in several cases (*9*, *38*).

To evaluate the ability of the algorithm to handle arbitrary edge lengths for precise design of wireframe objects of asymmetric and irregular geometries, we tested two different edge designs (Types II and III; see figs. S4 and S5) and compared them with a conventional discrete design assumption (Fig. 2B and Type I in fig. S4). For the discrete edge-length design, a quarter circle design consisted of various edges of 42-, 52-, 63-, and 84-bp length that requires seven unpaired T-bulge staples between every two neighboring edges in the vertices and zero unpaired nucleotides in the scaffold (Type I in fig. S4). AFM confirmed the successful assembly of this structure with high yield, which shows that all particles present boundary curvature and smooth overall shapes, with excess flexibility due to the use of edge lengths that are mismatched to the target geometry (figs. S4B and S6). For the two continuous edge designs (Types II and III in fig. S4B), the exact length of dsDNA required to fill the gap is calculated so that no excess flexibility is introduced ("continuous edge length" in Fig. 2B). AFM revealed that the direct connections without unpaired scaffold nucleotides were unable to fold properly to form the target shape (Type II in figs. S4B and S7). Therefore, unpaired nucleotides in the scaffold strand were instead introduced at the vertices in the Type III design to accommodate 5′- and 3′-end misalignment, using the rule described above (Type III in fig. S4B). AFM showed that the Type III design is optimal among the three cases (Fig. 2B and figs. S4B and S8), with an ability to accurately represent the target pattern using DNA with high structural fidelity. For all 2D wireframe structures with DX-based edges, the continuous edge length approach is used at irregular and boundary vertices, allowing for the design of highly irregular and asymmetric DNA structures (figs. S4 and S5).

Given the importance of overall mechanical stiffness and local geometric fidelity of the target shape, we first studied systematically the roles of the degree of the *N*-arm junctions, the overall size of the structure, and the internal mesh pattern including quadrilateral, constant direction triangular, and mixed-direction triangular meshes (Fig. 3 and figs. S9 to S27). Although we expected the *N*-arm junctions to be relatively flexible when the number of arms or the edge length increased due to the unpaired nucleotides present in vertices and cavities within the patterns, AFM results indicated that all the 2D DNA origami objects with DX-based edges were generally well formed, with minimal particle-to-particle heterogeneity structurally in-plane (Fig. 3 and figs. S28 to S36). In testing the three different mesh patterns, triangular meshes exhibited greater structural fidelity of the target shape than the quadrilateral mesh (Fig. 3C and fig. S34). Among the two triangular meshes tested, the mixed-direction version preserved symmetric *N*-way junctions best, with a less distorted shape than its counterparts (Fig. 3C and figs. S35 and S36). These results confirm the dual importance of both edge stiffness and internal wireframe geometry to endow geometric fidelity in 2D wireframe objects. A 2D finite element simulation of the curved arm geometry predicts (fig. S37) the relative flexibilities of the different mesh patterns in a manner that is consistent with the observed AFM data, further corroborating the importance of the choice of internal mesh to endow in-plane mechanical stiffness.

To test the generality and robustness of our autonomous design procedure, we applied it to design 15 objects with different types of internal meshes including triangular, quadrilateral, and other *N*-sided polygonal meshes, where *N* is the number of sides of the interior mesh element, and six designs were synthesized and characterized experimentally in each category of internal mesh type (Fig. 4). For the triangular mesh, square and honeycomb geometries were synthesized, which are symmetric and have uniform edge lengths, angles, and vertex degrees. For the quadrilateral meshes, symmetric rhombic tiling with multiway (two-, three-, four-, and six-way) arm junctions and a highly asymmetric quarter circle with unequal vertex angles and edge lengths for every edge were synthesized. Further, we applied our procedure to design and synthesize objects using polygons with larger numbers of

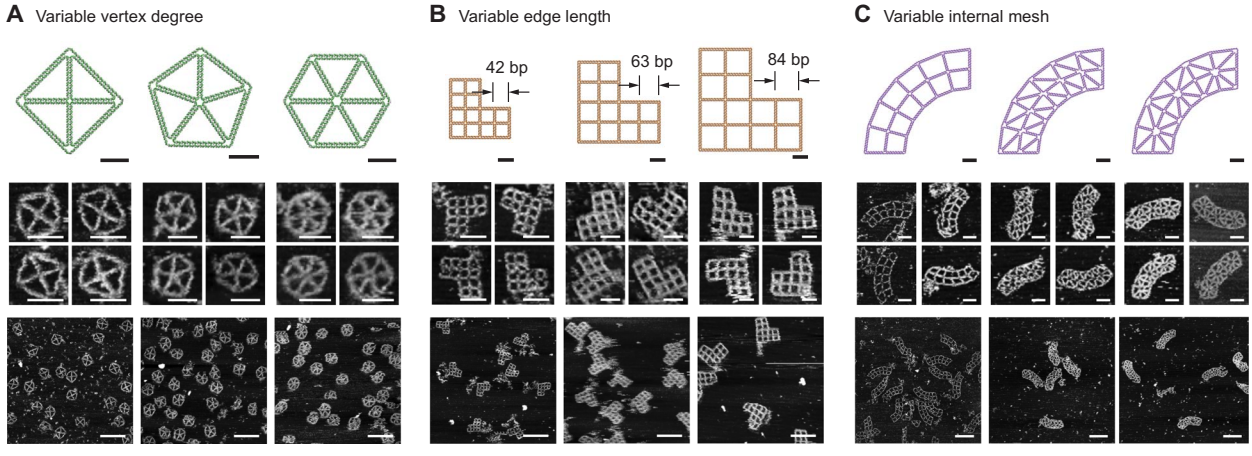

Fig. 3. Designing variable vertex numbers, edge lengths, and mesh patterns. (**A** to **C**) Variable vertex numbers consisting of four-, five-, or six-arm junctions (A), variable edge lengths of 42, 63, and 84 bp (B), and variable mesh patterns, including quadrilateral, constant direction triangular, and mixed-direction triangular meshes (C), can be used. A mechanical model of the curved arm geometry predicts flexibility using the (left) constant direction triangular mesh pattern, with increased in-plane mechanical stiffness introduced by the (right) mixed-direction triangular mesh pattern, demonstrating the importance of internal mesh geometry on overall in-plane flexibility (fig. S37). Scale bars, 20 nm (atomic structures) and 50 and 150 nm (zoom-in and zoom-out AFM images, respectively).

sides, including a Cairo pentagonal tiling consisting of five-sided polygonal meshes that have four long sides and one short side in the ratio $1:\sqrt{3}-1$ and a highly asymmetric lotus with three-, four-, five-, six-, seven-, and eight-sided polygonal meshes. Notably, all edges in the designed patterns have unique edge lengths determined automatically by the algorithm to match the target geometries by extending them to join one another at appropriate vertices (fig. S5). The minimum edge length needed to preserve two DX crossovers per edge is assigned to the shortest edge, which is then used to scale all other edges, equal to 42 bp in the present work, with the exception of the rhombic tiling with 84 bp, the quarter circle with 50 bp, and the lotus with 41 bp. Three different ssDNA scaffolds were used for sequence design and folding, with the required scaffold lengths and minimum edge lengths of all designed structures listed in table S1 and additional output design parameters provided in table S2. For self-assembly, the scaffold and corresponding staples were mixed together with appropriate stoichiometry (scaffold:staples = 1:20) in tris-acetate-EDTA (TAE)/Mg^{2+} buffer, and a monotonic temperature ramp was applied (see Materials and Methods for detailed methods). AFM shows successful formation of designed target objects at the single-particle level (Fig. 4 and fig. S38 to S53), with full-field AFM images revealing their high rate of proper formation (figs. S54 to S58 and table S3).

DISCUSSION

Our results demonstrate the fully autonomous sequence design of arbitrary free-form 2D geometries rendered using scaffolded DNA origami and a wireframe DX design motif. Using DX-based edges with a dual graph scaffold routing procedure enables arbitrary edge lengths, vertex degrees, and vertex angles to be programmed while maintaining local and global structural integrity as well as anticipated stability in physiological salt concentration (*11*), which are important to numerous applications in materials science and nanotechnology. Available online and as stand-alone open source software, PERDIX thereby broadly enables custom nanometer-scale templating of secondary molecules including dyes, nucleic acids, proteins, and semiconductor

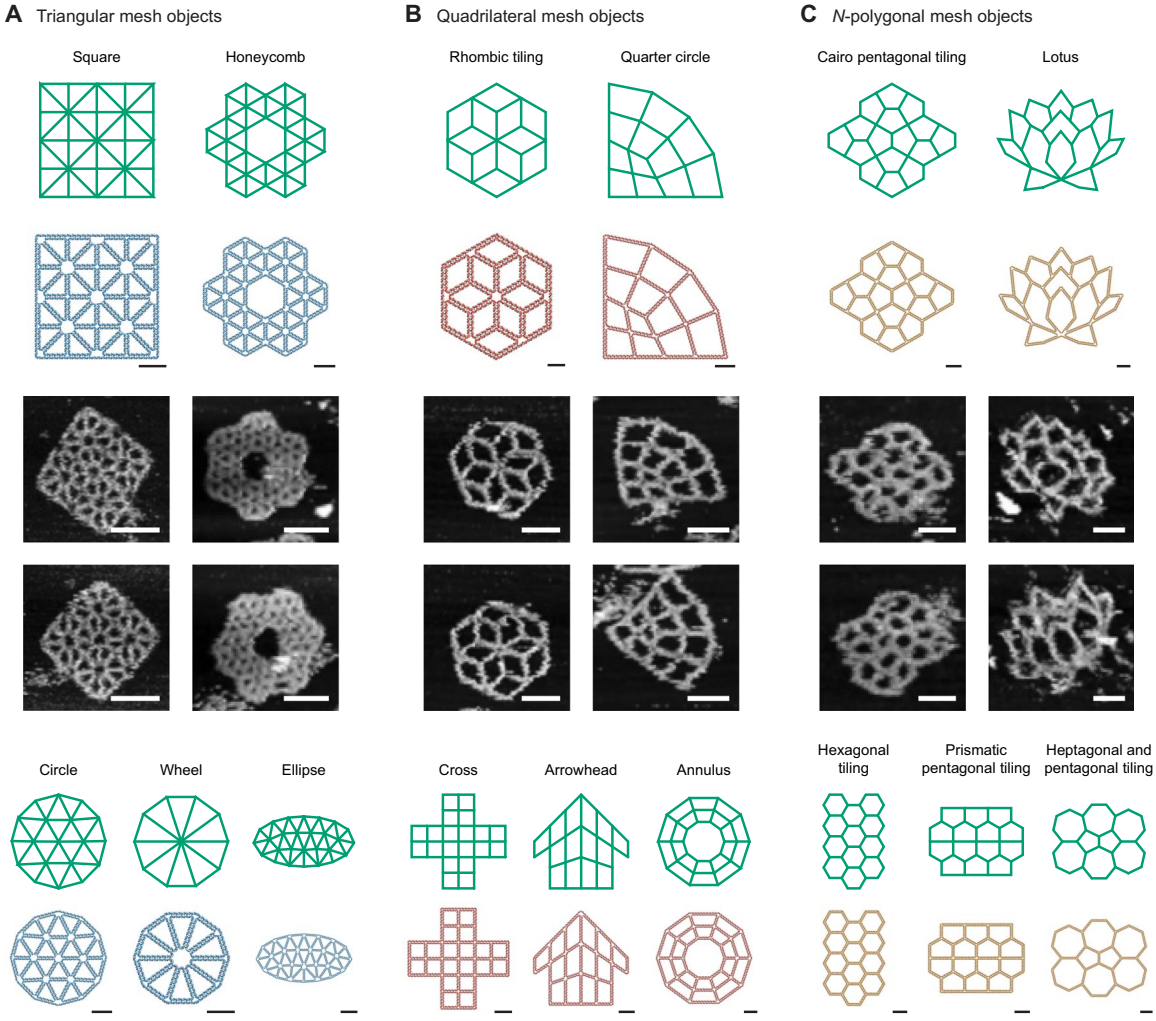

Fig. 4. Fully automatic sequence design of 15 diverse scaffolded origami wireframe objects. Target 2D wireframe objects and DNA-based atomic models of nanostructures are shown with (blue) triangular, (red) quadrilateral, and (yellow) *N*-polygonal meshes, where *N* is the number of sides of the discrete mesh element. Representative AFM images for a square lattice and honeycomb lattice with triangular cavities, a rhombic tiling and a quarter circle with quadrilateral cavities, and a Cairo pentagonal tiling and lotus with *N*-polygon cavities are shown. Scale bars, 20 nm (atomic structures) and 50 nm (AFM images).

nanocrystals for applications in nanophotonics, nanoscale energy transport, biomolecular sensing, structural studies, and cell-based binding assays. Output from PERDIX is compatible with the popular computer-aided design software caDNAno to facilitate manual base-level editing following automatic scaffold routing and staple sequence design for functionalization or other purposes. The algorithm used overcomes previous limitations in scaffold routing algorithms that constrained them to hybrid single-dual-duplex (*10*, *37*) or dual-duplex origami objects with discrete edge lengths (*11*), opening new opportunities for automated sequence design of 2D and 3D scaffolded DNA origami objects using variable edge types and multiway vertex designs.

MATERIALS AND METHODS

Materials

DNA origami staple strands were purchased in 384-well plates from Integrated DNA Technologies Inc. (www.IDTDNA.com) at 10- or 25-nmol synthesis scales in the format of solution. DNA oligos were normalized to 100 μM concentrations. Staple strands were mixed in equal volume from the corresponding wells and used directly without further purification. All staple sequences are listed in tables S4 to S18.

Three single-stranded circular DNA scaffold strands with lengths 2267, 5386, and 7249 nt were used (table S19). The 7249-nt DNA scaffold was produced using M13mp18 bacteriophage RF I DNA (New England Biolabs) following the same procedures, as described previously (*39*). The ΦX174 5386-nt DNA scaffold was purchased from New England Biolabs. The 2267-nt DNA scaffold was produced as the recombinant M13 bacteriophage DNA using the phagemid vector. The 2267-bp phagemid vector was generated by truncating the pBluescript II SK (+) vector using the Q5 Site-Directed Mutagenesis Kit (New England Biolabs). The 2267-bp phagemid vector was then cotransformed into DH5α competent cells with pSB4423 vector, a gift from S. Brown (Niels Bohr Institute, Denmark). The *Escherichia coli* colonies were inoculated into 2× YT (yeast extract tryptone) medium for overnight growth. The recombinant M13 bacteriophage and its genomic DNA were then purified with the same procedures, as described previously (*39*).

Origami assembly

All the origami structures were assembled by mixing 5 nM of its corresponding ssDNA scaffold with a 20 times molar excess of staple strands in 1× TAE/Mg^{2+} buffer [40 mM tris, 20 mM acetic acid, 2 mM EDTA, and 12.5 mM magnesium acetate (pH 8.0)]. The final volume of the mixture was 100 μl. The design details and sequences of the DNA oligos used to form each structure are shown in the Supplementary Materials. The mixture solutions were annealed in a polymerase chain reaction thermocycler (Eppendorf 6332000029 Thermal Cycler Eco) from 90° to 4°C in about 12 hours: 90° to 86°C at a rate of 4°C per 5 min, 85° to 70°C at a rate of 1°C per 5 min, 70° to 40°C at a rate of 1°C per 15 min, and 40°C to 25°C at 1°C per 10 min, held at 4°C in the end.

AFM imaging

The AFM imaging (figs. S6 to S8, S28 to S36, and S54 to S58) was conducted in "ScanAsyst mode in fluid" (Dimension FastScan, Bruker Corporation) with ScanAsyst-Fluid+ tips (Bruker Inc.). Two microliters of samples was deposited onto freshly cleaved mica (Ted Pella Inc.), and 0.5 to 1.0 μl of $NiCl_2$ with the concentration of 100 mM were added to the samples to fix the origami nanostructures on the mica surface. After waiting for about 30 s for sample adsorption to mica, 80 μl of 1× TAE/Mg^{2+} buffer was added to the samples, and an extra 40 μl of the same buffer was deposited on the AFM tip.

SUPPLEMENTARY MATERIALS

Supplementary material for this article is available at http://advances.sciencemag.org/cgi/content/full/5/1/eaav0655/DC1

Supplementary Materials and Methods

Fig. S1. Target geometry specification using piecewise continuous lines.

Fig. S2. Schematic illustrating key steps in the design algorithm PERDIX for a 2D plate composed of a triangular mesh.

Fig. S3. Scaffold and staple crossovers.

Fig. S4. Discrete versus continuous edge lengths for asymmetric and irregular shapes.

Fig. S5. Spanning the gap with precise lengths of dsDNA at an unequal vertex.

Fig. S6. AFM imaging of the DNA quarter circle wireframe lattice (Type I: discrete edges).

Fig. S7. AFM imaging of the DNA quarter circle wireframe lattice (Type II: continuous edges with no unpaired scaffold).

Fig. S8. AFM imaging of the DNA quarter circle wireframe lattice (Type III: continuous edges with unpaired scaffold nucleotides as needed).

Fig. S9. Nine target geometries used as input to the algorithm.

Fig. S10. Base pair models with the scaffold and staple double crossovers for nine diverse 2D wireframe lattice structures.

Fig. S11. Spanning trees of the dual graphs of the loop-crossover structures generated by the algorithm.

Fig. S12. Scaffold routing path of nine diverse 2D wireframe lattice structures generated by the algorithm.

Fig. S13. Staple design path of nine diverse 2D wireframe lattice structures generated by the algorithm.

Fig. S14. Cylindrical representations of nine diverse 2D wireframe lattice structures.

Fig. S15. Atomic models of nine diverse 2D wireframe lattice structures generated by the algorithm.

Fig. S16. Three different atomic representations of scaffolded DNA origami 2D wireframe structures with variable vertex degree.

Fig. S17. Three different atomic representations of scaffolded DNA origami 2D lattice structures of different scales.

Fig. S18. Three different atomic representations of scaffolded DNA origami 2D lattice structures designed with different mesh patterns.

Fig. S19. Exported scalable vector graphics (SVG) schematic of the DNA four-sided polygon.

Fig. S20. Exported SVG schematic of the DNA five-sided polygon.

Fig. S21. Exported SVG schematic of the DNA six-sided polygon.

Fig. S22. Exported SVG schematic of the 42-bp edge-length DNA L-shape wireframe lattice.

Fig. S23. Exported SVG schematic of the 63-bp edge-length DNA L-shape wireframe lattice.

Fig. S24. Exported SVG schematic of the 84-bp edge-length DNA L-shape wireframe lattice.

Fig. S25. Exported SVG schematic of the DNA curved-arm wireframe lattice (quadrilateral meshes).

Fig. S26. Exported SVG schematic of the DNA curved-arm wireframe lattice (triangular meshes).

Fig. S27. Exported SVG schematic of the DNA curved-arm wireframe lattice (mixed meshes).

Fig. S28. AFM imaging of the DNA four-sided polygon wireframe lattice.

Fig. S29. AFM imaging of the DNA five-sided polygon wireframe lattice.

Fig. S30. AFM imaging of the DNA six-sided polygon wireframe lattice.

Fig. S31. AFM imaging of the DNA 42-bp edge-length L-shape DNA wireframe lattice.

Fig. S32. AFM imaging of the DNA 63-bp edge-length L-shape wireframe lattice.

Fig. S33. AFM imaging of the DNA 84-bp edge-length L-shape DNA wireframe lattice.

Fig. S34. AFM imaging of the DNA curved-arm wireframe lattice (quadrilateral meshes).

Fig. S35. AFM imaging of the DNA curved-arm wireframe lattice (triangular meshes).

Fig. S36. AFM imaging of the DNA curved-arm wireframe lattice (mixed meshes).

Fig. S37. Truss-like finite element simulation.

Fig. S38. Fifteen target geometries used as input to the algorithm.

Fig. S39. Base pair models with the scaffold and staple double crossovers for 15 diverse 2D wireframe lattice structures.

Fig. S40. Fifteen spanning trees of the dual graph of the loop-crossover structures generated by the algorithm.

Fig. S41. Scaffold-routing path of 15 diverse 2D wireframe lattice structures generated by the algorithm.

Fig. S42. Staple design path of 15 diverse 2D wireframe lattice structures generated by the algorithm.

Fig. S43. Cylindrical representations of 15 diverse 2D wireframe lattice structures.

Fig. S44. Atomic models of 15 diverse 2D wireframe lattice structures generated by the algorithm.

Fig. S45. Three different atomic representations of scaffolded DNA origami 2D wireframe structures with triangular meshes.
Fig. S46. Three different atomic representations of scaffolded DNA origami 2D wireframe structures with quadrilateral meshes.
Fig. S47. Three different atomic representations of scaffolded DNA origami 2D wireframe structures with *N*-polygonal meshes.
Fig. S48. Exported SVG schematic of the square wireframe lattice.
Fig. S49. Exported SVG schematic of the honeycomb wireframe lattice.
Fig. S50. Exported SVG schematic of the DNA rhombic tiling lattice.
Fig. S51. Exported SVG schematic of the DNA quarter circle wireframe lattice.
Fig. S52. Exported SVG schematic of the DNA Cairo pentagonal tiling.
Fig. S53. Exported SVG schematic of the DNA lotus wireframe lattice.
Fig. S54. AFM imaging of the DNA square wireframe lattice.
Fig. S55. AFM imaging of the DNA honeycomb wireframe lattice.
Fig. S56. AFM imaging of the DNA rhombic tiling wireframe lattice.
Fig. S57. AFM imaging of the DNA Cairo pentagonal tiling wireframe lattice.
Fig. S58. AFM imaging of the DNA lotus wireframe lattice.
Table S1. Required scaffold lengths for 24 rendered DNA lattice structures.
Table S2. Output from of the automatic sequence design for DNA origami 2D wireframe structures.
Table S3. Folding yields determined by counting well-folded particles from AFM imaging.
Table S4. Staple sequence for 84-bp edge-length DNA four-sided polygon origami folding.
Table S5. Staple sequence for 84-bp edge-length DNA five-sided polygon origami folding.
Table S6. Staple sequence for 84-bp edge-length DNA six-sided polygon origami folding.
Table S7. Staple sequence for 42-bp edge-length DNA L-shape origami folding.
Table S8. Staple sequence for 63-bp edge-length DNA L-shape origami folding.
Table S9. Staple sequence for 84-bp edge-length DNA L-shape origami folding.
Table S10. Staple sequence for DNA curved-beam origami folding (quadrilateral mesh pattern).
Table S11. Staple sequence for DNA curved-beam origami folding (triangular mesh pattern).
Table S12. Staple sequence for DNA curved-beam origami folding (mixed mesh pattern).
Table S13. Staple sequence for 42-bp edge-length DNA plate origami folding.
Table S14. Staple sequence for 42-bp edge-length DNA honeycomb origami folding.
Table S15. Staple sequence for 84-bp edge-length DNA rhombic tiling origami folding.
Table S16. Staple sequence for DNA quarter circle origami folding.
Table S17. Staple sequence for DNA Cairo pentagonal tiling origami folding.
Table S18. Staple sequence for DNA lotus origami folding.
Table S19. Sequences for the 7249-nt (#1), 5386-nt (#2), and 2267-nt (#3) length scaffolds used.
Movie S1. PERDIX run.
Movie S2. PERDIX boundary design.
Movie S3. PERDIX boundary and internal design.
Movie S4. Atomic models: Different meshes.
Movie S5. Atomic models: *N*-arm.
Movie S6. Atomic models: L-shape.
Movie S7. Atomic models: Curved arm.
Data file S1. PERDIX software package
Data file S2. PERDIX software documentation
References (*40*–*46*)

REFERENCES AND NOTES

1. N. C. Seeman, Nucleic acid junctions and lattices. *J. Theor. Biol.* **99**, 237–247 (1982).
2. E. Winfree, F. Liu, L. A. Wenzler, N. C. Seeman, Design and self-assembly of two-dimensional DNA crystals. *Nature* **394**, 539–544 (1998).
3. P. W. K. Rothemund, Folding DNA to create nanoscale shapes and patterns. *Nature* **440**, 297–302 (2006).
4. S. M. Douglas, H. Dietz, T. Liedl, B. Högberg, F. Graf, W. M. Shih, Self-assembly of DNA into nanoscale three-dimensional shapes. *Nature* **459**, 414–418 (2009).
5. H. Dietz, S. M. Douglas, W. M. Shih, Folding DNA into twisted and curved nanoscale shapes. *Science* **325**, 725–730 (2009).
6. C. E. Castro, F. Kilchherr, D.-N. Kim, E. Lin Shiao, T. Wauer, P. Wortmann, M. Bathe, H. Dietz, A primer to scaffolded DNA origami. *Nat. Methods* **8**, 221–229 (2011).
7. D. Han, S. Pal, J. Nangreave, Z. Deng, Y. Liu, H. Yan, DNA origami with complex curvatures in three-dimensional space. *Science* **332**, 342–346 (2011).
8. K. E. Dunn, F. Dannenberg, T. E. Ouldridge, M. Kwiatkowska, A. J. Turberfield, J. Bath, Guiding the folding pathway of DNA origami. *Nature* **525**, 82–86 (2015).
9. F. Zhang, S. Jiang, S. Wu, Y. Li, C. Mao, Y. Liu, H. Yan, Complex wireframe DNA origami nanostructures with multi-arm junction vertices. *Nat. Nanotechnol.* **10**, 779–784 (2015).
10. E. Benson, A. Mohammed, J. Gardell, S. Masich, E. Czeizler, P. Orponen, B. Högberg, DNA rendering of polyhedral meshes at the nanoscale. *Nature* **523**, 441–444 (2015).
11. R. Veneziano, S. Ratanalert, K. Zhang, F. Zhang, H. Yan, W. Chiu, M. Bathe, Designer nanoscale DNA assemblies programmed from the top down. *Science* **352**, 1534 (2016).
12. K. Lund, A. J. Manzo, N. Dabby, N. Michelotti, A. Johnson-Buck, J. Nangreave, S. Taylor, R. Pei, M. N. Stojanovic, N. G. Walter, E. Winfree, H. Yan, Molecular robots guided by prescriptive landscapes. *Nature* **465**, 206–210 (2010).
13. J. Song, Z. Li, P. Wang, T. Meyer, C. Mao, Y. Ke, Reconfiguration of DNA molecular arrays driven by information relay. *Science* **357**, eaan3377 (2017).
14. K. F. Wagenbauer, C. Sigl, H. Dietz, Gigadalton-scale shape-programmable DNA assemblies. *Nature* **552**, 78–83 (2017).
15. E. Kopperger, J. List, S. Madhira, F. Rothfischer, D. C. Lamb, F. C. Simmel, A self-assembled nanoscale robotic arm controlled by electric fields. *Science* **359**, 296–301 (2018).
16. B. Wei, M. Dai, P. Yin, Complex shapes self-assembled from single-stranded DNA tiles. *Nature* **485**, 623–626 (2012).
17. L. L. Ong, N. Hanikel, O. K. Yaghi, C. Grun, M. T. Strauss, P. Bron, J. Lai-Kee-Him, F. Schueder, B. Wang, P. Wang, J. Y. Kishi, C. A. Myhrvold, A. Zhu, R. Jungmann, G. Bellot, Y. Ke, P. Yin, Programmable self-assembly of three-dimensional nanostructures from 10,000 unique components. *Nature* **552**, 72–77 (2017).
18. G. Tikhomirov, P. Petersen, L. Qian, Fractal assembly of micrometre-scale DNA origami arrays with arbitrary patterns. *Nature* **552**, 67–71 (2017).
19. H. T. Maune, S. P. Han, R. D. Barish, M. Bockrath, W. A. Goddard III, R. P. W. Goddard, E. Winfree, Self-assembly of carbon nanotubes into two-dimensional geometries using DNA origami templates. *Nat. Nanotechnol.* **5**, 61–66 (2010).
20. A. Kuzyk, R. Schreiber, Z. Fan, G. Pardatscher, E.-M. Roller, A. Högele, F. C. Simmel, A. O. Govorov, T. Liedl, DNA-based self-assembly of chiral plasmonic nanostructures with tailored optical response. *Nature* **483**, 311–314 (2012).
21. Z. Deng, C. Mao, DNA-templated fabrication of 1D parallel and 2D crossed metallic nanowire arrays. *Nano Lett.* **3**, 1545–1548 (2003).
22. H. Yan, S. H. Park, G. Finkelstein, J. H. Reif, T. H. LaBean, DNA-templated self-assembly of protein arrays and highly conductive nanowires. *Science* **301**, 1882–1884 (2003).
23. W. Sun, E. Boulais, Y. Hakobyan, W. Li Wang, A. Guan, M. Bathe, P. Yin, Casting inorganic structures with DNA molds. *Science* **346**, 1258361 (2014).
24. S. Helmi, C. Ziegler, D. J. Kauert, R. Seidel, Shape-controlled synthesis of gold nanostructures using DNA origami molds. *Nano Lett.* **14**, 6693–6698 (2014).
25. Z. Jin, W. Sun, Y. Ke, C.-J. Shih, G. L. C. Paulus, Q. H. Wang, B. Mu, P. Yin, M. S. Strano, Metallized DNA nanolithography for encoding and transferring spatial information for graphene patterning. *Nat. Commun.* **4**, 1663 (2013).
26. A. Shaw, V. Lundin, E. Petrova, F. Fördős, E. Benson, A. Al-Amin, A. Herland, A. Blokzijl, B. Högberg, A. I. Teixeira, Spatial control of membrane receptor function using ligand nanocalipers. *Nat. Methods* **11**, 841–846 (2014).
27. N. V. Voigt, T. Tørring, A. Rotaru, M. F. Jacobsen, J. B. Ravnsbaek, R. Subramani, W. Mamdouh, J. Kjems, A. Mokhir, F. Besenbacher, K. V. Gothelf, Single-molecule chemical reactions on DNA origami. *Nat. Nanotechnol.* **5**, 200–203 (2010).
28. É. Boulais, N. P. D. Sawaya, R. Veneziano, A. Andreoni, J. L. Banal, T. Kondo, S. Mandal, S. Lin, G. S. Schlau-Cohen, N. W. Woodbury, H. Yan, A. Aspuru-Guzik, M. Bathe, Programmed coherent coupling in a synthetic DNA-based excitonic circuit. *Nat. Mater.* **17**, 159–166 (2018).
29. S. M. Douglas, I. Bachelet, G. M. Church, A logic-gated nanorobot for targeted transport of molecular payloads. *Science* **335**, 831–834 (2012).
30. S. Li, Q. Jiang, S. Liu, Y. Zhang, Y. Tian, C. Song, J. Wang, Y. Zou, G. J. Anderson, J.-Y. Han, Y. Chang, Y. Liu, C. Zhang, L. Chen, G. Zhou, G. Nie, H. Yan, B. Ding, Y. Zhao, A DNA nanorobot functions as a cancer therapeutic in response to a molecular trigger in vivo. *Nat. Biotechnol.* **36**, 258–264 (2018).
31. A. Gopinath, E. Miyazono, A. Faraon, P. W. K. Rothemund, Engineering and mapping nanocavity emission via precision placement of DNA origami. *Nature* **535**, 401–405 (2016).
32. B. Shen, V. Linko, K. Tapio, S. Pikker, T. Lemma, A. Gopinath, K. V. Gothelf, M. A. Kostiainen, J. J. Toppari, Plasmonic nanostructures through DNA-assisted lithography. *Sci. Adv.* **4**, eaap8978 (2018).
33. R. Veneziano, T. R. Shepherd, S. Ratanalert, L. Bellou, C. Tao, M. Bathe, In vitro synthesis of gene-length single-stranded DNA. *Sci. Rep.* **8**, 6548 (2018).
34. F. Praetorius, B. Kick, K. L. Behler, M. N. Honemann, D. Weuster-Botz, H. Dietz, Biotechnological mass production of DNA origami. *Nature* **552**, 84–87 (2017).
35. S. M. Douglas, A. H. Marblestone, S. Teerapittayanon, A. Vazquez, G. M. Church, W. M. Shih, Rapid prototyping of 3D DNA-origami shapes with caDNAno. *Nucleic Acids Res.* **37**, 5001–5006 (2009).
36. S. Williams, K. Lund, C. Lin, P. Wonka, S. Lindsay, H. Yan, Tiamat: A Three-Dimensional Editing Tool for Complex DNA Structures, in *DNA Computing*, A. Goel, F. C. Simmel, P. Sosík, Eds. (Springer, 2008), vol. 5347, pp. 90–101.
37. E. Benson, A. Mohammed, A. Bosco, A. I. Teixeira, P. Orponen, B. Högberg, Computer-aided production of scaffolded DNA nanostructures from flat sheet meshes. *Angew. Chem. Int. Ed.* **55**, 8869–8872 (2016).
38. N. P. Agarwal, M. Matthies, B. Joffroy, T. L. Schmidt, Structural transformation of wireframe DNA origami via DNA polymerase assisted gap-filling. *ACS Nano* **12**, 2546–2553 (2018).

39. G. Bellot, M. A. McClintock, J. J. Chou, W. M. Shih, DNA nanotubes for NMR structure determination of membrane proteins. *Nat. Protoc.* **8**, 755–770 (2013).
40. P.-O. Persson, G. Strang, A simple mesh generator in MATLAB. *SIAM Rev.* **46**, 329–345 (2004).
41. S. Gillies, *Shapely: Manipulation and Analysis of Geometric Objects*, 2007; https://github.com/Toblerity/Shapely.
42. D. Falck, B. Collette, *FreeCAD* (Packt Publishing, Birmingham Mumbai, 2012).
43. M. C. Murphy, I. Rasnik, W. Cheng, T. M. Lohman, T. Ha, Probing single-stranded DNA conformational flexibility using fluorescence spectroscopy. *Biophys. J.* **86**, 2530–2537 (2004).
44. J. A. Ellis-Monaghan, A. McDowell, I. Moffatt, G. Pangborn, DNA origami and the complexity of Eulerian circuits with turning costs. *Nat. Comput.* **14**, 491–503 (2015).
45. E. F. Pettersen, T. D. Goddard, C. C. Huang, G. S. Couch, D. M. Greenblatt, E. C. Meng, T. E. Ferrin, UCSF Chimera—A visualization system for exploratory research and analysis. *J. Comput. Chem.* **25**, 1605–1612 (2004).
46. K. Pan, D.-N. Kim, F. Zhang, M. R. Adendorff, H. Yan, M. Bathe, Lattice-free prediction of three-dimensional structure of programmed DNA assemblies. *Nat. Commun.* **5**, 5578 (2014).

Acknowledgments

Funding: We gratefully acknowledge funding from the NSF (CCF-1564025 and CMMI-1334109) and the Office of Naval Research (ONR) (N000141210621) to H.J., T.S., S.R., and M.B. and the ONR (N000141512689); the NSF (1360635, 1547962, 1563799, and 1334109), the Army Research Office (ARO) (W911NF1210420); and the National Institute of Allergy and Infectious Diseases (NIAID) (AI125827) to F.Z., X.Q., and H.Y. **Author contributions:** H.J. and M.B. conceived the free-form autonomous design approach. H.J. implemented the autonomous design algorithm and processed the results to make the figures. T.S. and S.R. provided feedback on the implementation and design procedure. H.J. and T.S. implemented the Web server. F.Z. and H.Y. conceived the experimental assay. F.Z. and X.Q. implemented the experimental assay, generated the experimental data, and processed the results to make the experimental figures. H.J., F.Z., T.S., and M.B. wrote the manuscript. M.B. supervised the project. All authors commented on and edited the manuscript. **Competing interests:** H.J., T.S., S.R., and M.B. are inventors on a pending patent related to this work, filed on 27 April 2017 (PCT/US2017/029891). The other authors declare that they have no other competing interests. **Data and materials availability:** The source code is released with GPL-3.0 license through GitHub (http://github.com/lcbb/PERDIX). All data needed to evaluate the conclusions in the paper are present in the paper and/or the Supplementary Materials. Additional data related to this paper may be requested from the authors.

Submitted 10 August 2018
Accepted 21 November 2018
Published 4 January 2019
10.1126/sciadv.aav0655

Citation: H. Jun, F. Zhang, T. Shepherd, S. Ratanalert, X. Qi, H. Yan, M. Bathe, Autonomously designed free-form 2D DNA origami. *Sci. Adv.* **5**, eaav0655 (2019).